
Improved On-Shot Focal-Spot Measurement on OMEGA EP Using Phase-Retrieval-Enhanced Wavefront Measurements

Introduction

Intensity at the target plane is a critical parameter in many inertial confinement fusion (ICF) experiments conducted on the short-pulse OMEGA EP laser.¹ Measuring the focal-spot intensity at the target plane on a high-energy shot, however, is a challenging task. Remote camera measurements can be made with a sampled diagnostic beam, but it is not easy to account for the effect of the final optics that focus the beam to target and the optics for the diagnostic. For OMEGA EP, a remote wavefront-measurement system has been developed to make on-shot target-plane focal-spot predictions for the short-pulse beams.² Limitations in the wavefront sensor and errors in the calibration and on-shot measurement, however, can lead to erroneous wavefront measurements that in turn yield poor focal-spot predictions.

In many applications where wavefront information is desired, phase-retrieval techniques have been effective in estimating wavefront based on a series of intensity measurements.^{3–7} Often, these measurements are made simultaneously in two different planes, e.g., a pupil plane and a far-field plane, or two or more far-field planes at different defocus distances. A variety of algorithms have been used to estimate the phases of the optical fields in these planes based on the rules of propagation between them. These can generally be classified into two categories: iterative-transform methods and gradient-search methods.⁵ In the former category, an initial guess is made about the phase profile in one plane, and the field is propagated back and forth between the planes with the magnitude of the field being replaced with the measured value and the phase being based on the calculated phase at each iteration.³ In the latter category, a merit function is produced and minimized by utilizing its gradient over a discrete set of variables.^{5,6} Gradient-search algorithms can be point-by-point (independently varying the wavefront at discrete points over the planes of interest) or modal (modifying the coefficients of a modal expansion of the wavefront).

In this article, we demonstrate the use of phase retrieval to improve the focal-spot measurement on OMEGA EP. As

a result of this work, the on-shot focal-spot measurement has been improved to the point that it reliably matches direct measurements of the focal-spot intensity at low energy. This article is organized as follows: OMEGA EP and the on-shot target-plane focal-spot measurement technique are reviewed and initial performance of the focal-spot measurement is assessed; four problems with the focal-spot measurements are described and phase-retrieval techniques for mitigating them are described; the results of applying these improvements to the focal-spot measurement are described with the accuracy and reliability assessed over a population of shot data; and finally, conclusions are presented.

Overview of Focal-Spot Measurement

The focal-spot diagnostic (FSD) was deployed on OMEGA EP to characterize on-shot, target-plane fluence distributions for the short-pulse beamlines. The OMEGA EP short-pulse system uses optical parametric chirped-pulse amplification (OPCPA) to generate a high-energy, high-peak-power laser pulse.¹ A seed pulse is stretched and amplified using both parametric amplification and conventional amplification in the front-end laser system and large-aperture beamline. At its fully amplified level, the beam is stretched to approximately 1-ns duration and amplified to multiple kilojoules. It then propagates into a grating compression chamber (GCC), a large vacuum chamber containing a four-grating pulse compression system, where it is compressed to between 700 fs (best compression) and 100 ps.

Figure 124.31 shows a diagram of one of the compressors in the OMEGA EP short-pulse system, indicating the location of key diagnostics relative to the beam for the on-shot focal-spot measurement. After undergoing amplification, pulse recompression, and wavefront correction, the beam propagates to a leaky diagnostic mirror within the GCC. A small percentage of the beam (~0.5%) transmits through the diagnostic mirror and is provided to a suite of laser diagnostics—the short-pulse diagnostics package (SPDP). The main beam, i.e., the portion reflected from the diagnostic mirror, is transported to the target chamber via a series of mirrors and focused by an $f/2$ off-axis parabola (OAP).

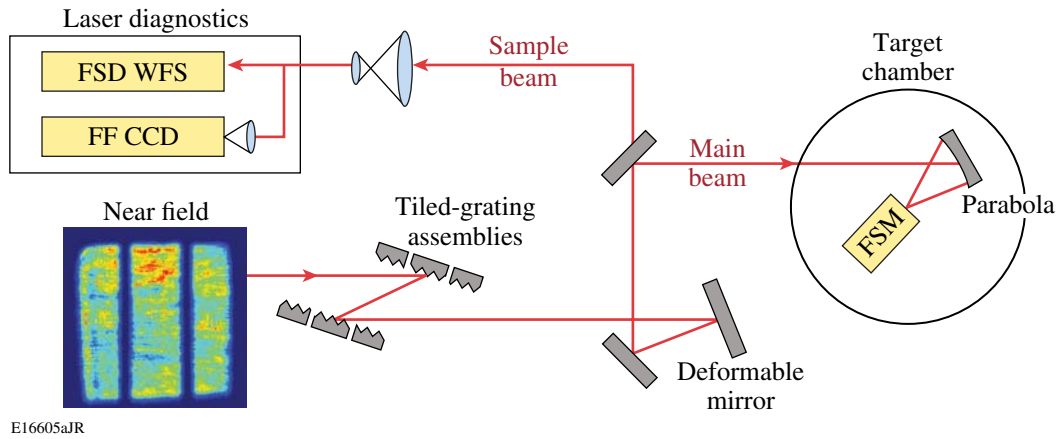


Figure 124.31

A diagram of the OMEGA EP short-pulse system indicates the location of key diagnostics relative to the beam for on-shot focal-spot measurement. After undergoing amplification, pulse recompression, and wavefront correction, the main OMEGA EP beam propagates to a leaky diagnostic mirror within the vacuum grating compression chamber. A small percentage of the beam (~0.5%) leaks through the diagnostic mirror and is provided to a suite of laser diagnostics, including the focal-spot diagnostic wavefront sensor (FSD WFS) and a far-field camera (FF CCD). The main beam is transported to the target chamber and focused at target chamber center by an $f/2$ off-axis parabola. For low-energy qualification shots, a focal-spot microscope (FSM) was inserted to directly image the focal spot at the target plane.

The FSD is a high-resolution wavefront sensor installed in the SPDP,⁸ denoted FSD WFS in Fig. 124.31. The FSD wavefront sensor provides a full measurement of the (temporally and spectrally averaged) near-field amplitude and phase of the sample beam that can be numerically propagated to calculate the focal-spot fluence distribution.⁹

In close proximity to the FSD is a 16-bit, cooled, far-field charge-coupled-device (CCD) camera (FF CCD in Fig. 124.31) that records the focal-spot fluence distribution of the sample beam. Both the FSD and this FF CCD acquire data on every OMEGA EP shot. In addition, for some low-energy shots, a focal-spot microscope (FSM) has been inserted into the target chamber to directly image the focal spot at the target plane

onto another 16-bit cooled CCD camera.² These two cameras provide the direct focal-spot intensity measurements that are used as inputs to the phase-retrieval algorithms discussed in this article. The image data from both of these CCD's also provide a check of the quality of the phase-retrieval results.

One of the challenges of this approach to measuring the target-plane focal spot is the indirect nature of the wavefront measurement. The measurement requires a careful calibration of the FSD wavefront sensor to “transfer” (or reference) the wavefront of the sample beam measured in the SPDP to the wavefront of the main beam inside the target chamber. The FSD is calibrated using the two-step process described in detail in Ref. 2 and illustrated in Fig. 124.32. A brief description is

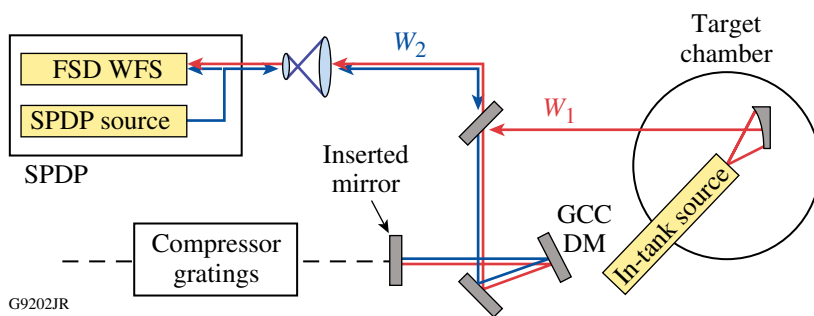


Figure 124.32

The FSD is calibrated using the two-step process illustrated. In the first step, a laser source is inserted into the target chamber with a focus at target chamber center (TCC) and propagated backward to the FSD wavefront sensor via an inserted alignment mirror. The wavefront W_1 is measured in this configuration. Next, a laser source on the SPDP diagnostic table is propagated to the alignment diagnostic mirror (DM) and back to the wavefront sensor, where the wavefront contribution W_2 is measured. The transfer wavefront, essentially $W_1 - W_2$ with pre-measured source wavefront contributions also compensated, is added to on-shot wavefront measurements to obtain the wavefront error of the main beam inside the target chamber.

given here. In the first step, an in-tank laser source is focused to target chamber center (TCC) and propagated backward to the FSD wavefront sensor via an inserted alignment mirror. The wavefront W_1 is measured in this configuration. Next, a laser source in the SPDP is propagated to the alignment mirror and back to the FSD wavefront sensor, where the wavefront contribution W_2 is measured.

A “transfer wavefront” is defined essentially as $W_1 - W_2$. When added to the directly measured sample-beam wavefront, the transfer wavefront removes the wavefront contributions from the diagnostic beam path (between the diagnostic mirror and the FSD sensor) and adds the wavefront contributions from the beam transport to the target (between the diagnostic mirror and the target). Additionally, another correction factor is applied, based on the pre-characterized wavefront contributions of the two sources used for the calibration. The measurement of the wavefront contributions from these two sources is thought to be one of the primary sources of error in the calibration process.

To evaluate the focal-spot measurement, the far-field distribution calculated from the FSD near-field measurement is compared to the directly measured far field from the appropriate CCD camera (either the far-field CCD or the FSM). The agreement is quantified by the cross-correlation

$$C = \frac{\max \left[\iint F_{\text{FSD}}(x - \Delta_x, y - \Delta_y) F_{\text{CCD}}(x, y) dx dy \right]}{\left[\left(\iint F_{\text{FSD}}^2 dx dy \right) \left(\iint F_{\text{CCD}}^2 dx dy \right) \right]^{1/2}}, \quad (1)$$

where F_{FSD} and F_{CCD} are the far-field fluence distributions from the FSD and the camera, respectively. The cross-correlation is normalized in such a way that a perfect agreement results in a value of unity. In practice, a value $C > 0.9$ has been found to normally indicate an acceptable measurement.

Initially, when focal-spot intensity distributions were measured using the FSD wavefront sensor, the results were often quite poor. An example of this is shown in Fig. 124.33, where the focal spot of the sample beam as predicted by the FSD wavefront sensor [Fig. 124.33(a)] and measured by the SPDP far-field CCD camera [Fig. 124.33(b)] are displayed side by side. Both focal spots are plotted as normalized fluence (fluence divided by total energy, in cm^{-2}) over a square $100\text{-}\mu\text{rad}$ field of view. The poor agreement ($C = 0.71$) between these two diagnostics, which measured the same beam in close proximity, illustrates the challenge of the on-shot focal-spot measurement.

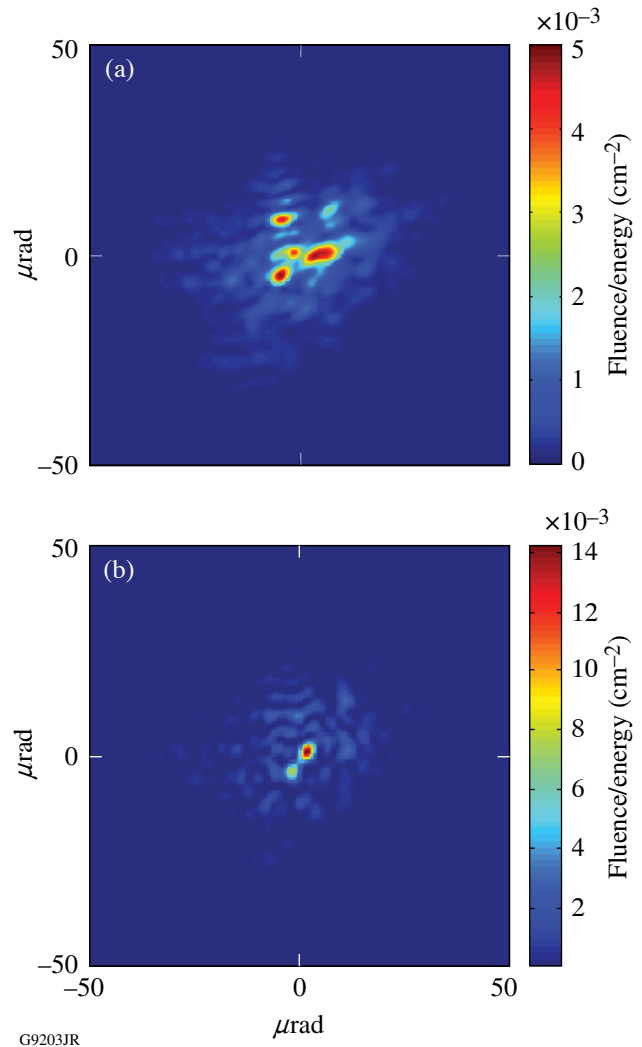


Figure 124.33

An example of an early focal-spot measurement of the sample beam. The color map (a) is a direct measurement using the FF CCD camera, while (b) shows the initial result using the FSD near-field measurement. Both focal spots are expressed in normalized fluence (fluence divided by total energy, in cm^{-2}) and are plotted over a square $100\text{-}\mu\text{rad}$ field of view. The poor agreement by two diagnostics measuring the same beam in close proximity illustrates the challenge of the on-shot focal-spot measurement.

Four problems, discussed in further detail in the next section, have led to poor FSD focal-spot measurements of the type shown in Fig. 124.33. The first problem is a fixed wavefront error between the FSD wavefront measurement and the wavefront incident on the FF CCD. The second is the inability of a Shack–Hartmann wavefront sensor to measure the mean relative wavefront (piston phase) between discrete beam segments that are generated by the tiled-grating compressor. The third problem is chromatic wavefront errors that are undetectable by the Shack–Hartmann wavefront sensor and have a significant

effect on the fidelity of the focal spot. Finally, fixed errors in the FSD calibration process further degrade the quality of the remote focal-spot measurement at the target plane. Each of these problems has been mitigated by retrieving phase information embedded within the focal-spot measurements from the FF CCD and the focal-spot microscope.

Phase-Retrieval Applications and Results

1. Phase Retrieval of SPDP Transfer Wavefront from Multiple Measurements

Whereas the FSD wavefront sensor is in very close proximity to the FF CCD camera, differences between the measured wavefront and the actual wavefront of the focusing beam at the FF CCD must be considered. First, the Shack–Hartmann wavefront measurement is a relative measurement against a reference beam. Wavefront errors in the reference beam translate directly into errors in the measured wavefront. For the FSD, a reference wavefront was acquired using an alignment laser located in the diagnostic package (the SPDP source in Fig. 124.32), reflected from a reference mirror back into the FSD. In principle, this removes the wavefront contributions from the four-element relay lens used to image the pupil onto the FSD wavefront sensor. Wavefront error in the reference laser itself, however, will introduce errors in the reference measurement. These errors were characterized separately and compensated for; however the accumulation of errors can be significant.

In addition, the optics between the FSD and the FF CCD must be considered. Aside from two planar reflective optics, a four-element focusing lens produces a far-field image on the sensor plane of the FF CCD. There is also a window on the camera (wedged and tilted to remove artifacts) as well as various neutral density filters, but these are all in close proximity to the far-field plane and therefore have little effect on the focal spot.

To account for these errors, an SPDP transfer wavefront analogous to the transfer wavefront used to produce target-plane wavefront measurements was defined. The SPDP transfer wavefront is a static quantity (assuming no system configuration changes) that is added to every FSD wavefront sensor measurement to obtain the wavefront at the exit pupil of the FF CCD lens. It was inferred from simultaneous FSD and FF CCD measurements over multiple laser shots using phase retrieval.

The classical iterative transform methods of phase retrieval were attempted on this problem but were generally unsuccessful. These included the so-called Gerchberg–Saxton algorithm³ and various refinements such as the input–output algorithm of Fienup.⁵ These algorithms produced nonphysical results

in which zeros would appear in the near field around which the phase would process continuously over a 2π range. When the phase was unwrapped, branch cuts would be required, leading to unphysical discontinuities in the wavefront. The problem appears to have been caused by a combination of polychromatic effects and a small incoherent background in the far-field measurements.

To improve focal-spot predictions, a modal phase-retrieval method that has proven to be successful and robust was employed. It is based closely on a gradient-search algorithm reported by Fienup.⁶ A block diagram of the algorithm is shown in Fig. 124.34. The inputs to the algorithm are the measured near-field intensity and wavefront from the FSD wavefront sensor and the measured focal-spot intensity from the FF CCD camera. The algorithm produces a single low-order SPDP transfer wavefront expressed as a two-dimensional Legendre polynomial, as well as the piston phases in the left and right beam segments (as discussed in the following subsection). Multiple shots are evaluated simultaneously to improve accuracy.

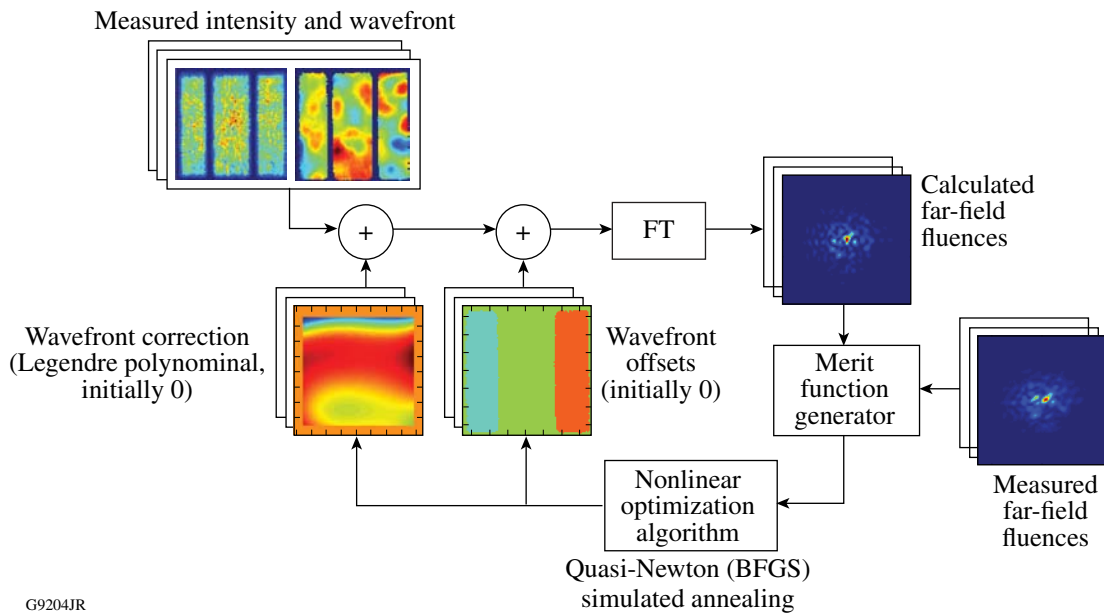
The algorithm proceeds from the near-field intensities and wavefronts measured by the FSD wavefront sensor. The current SPDP transfer wavefront is added to all the wavefronts, and the wavefront offsets are added to the outer tiles of the appropriate wavefronts. The far-field fluence distributions are then calculated from the near-field intensity and the corrected wavefront. These are compared to the measured values to generate a merit function, which is based on the root-sum-square (rss) error,

$$\text{rss error} = \left\{ \iint [F_{\text{FSD}}(x,y) - F_{\text{CCD}}(x,y)]^2 dx dy \right\}^{1/2}. \quad (2)$$

The rss errors from all shots are summed to produce an overall merit function that takes into account errors over the entire data set.

A nonlinear optimization algorithm is employed to modify the optimization parameters for the subsequent iterations. In most cases, a quasi-Newton, Broyden–Fletcher–Goldfarb–Shanno (BFGS) algorithm¹⁰ is used, which is a true gradient-search algorithm. Alternatively, to attempt to find a global solution, a simulated annealing algorithm has initially been employed¹¹ to identify the approximate solution, followed by a gradient search algorithm to obtain a more-accurate estimate. The algorithm continues until the merit function is minimized.

This modal phase-retrieval algorithm was used to measure the SPDP transfer wavefront for the FSD sensors in both the upper and lower compressors on OMEGA EP. A fourth-order



G9204JR

Figure 124.34

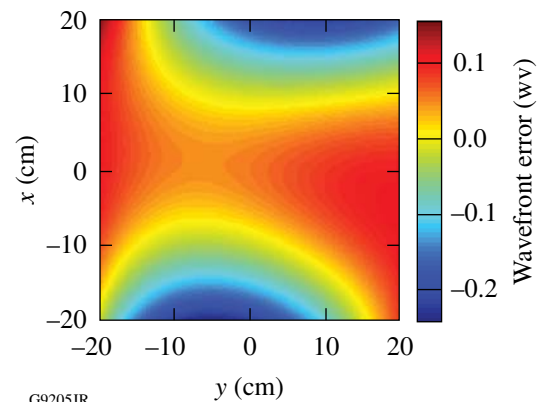
A block diagram illustrating the modal phase-retrieval algorithm used to measure the SPDP transfer wavefront. The inputs to the algorithm are the measured near-field intensity and wavefront from the FSD wavefront sensor and the measured focal-spot intensity from the FF CCD camera. Multiple shots are evaluated simultaneously to improve accuracy. The far-field fluence distributions are calculated from the measured near fields using Fourier transforms (FT) and compared to the measured values to generate a merit function. This merit function is minimized by using a nonlinear optimization algorithm to vary the SPDP transfer wavefront (estimated as a Legendre polynomial) and the average phase in the outer beam segments for each shot. The SPDP transfer wavefront and average phases are added to the original measurements in the subsequent iteration. The algorithm continues until the merit function is minimized.

Legendre polynomial was used to estimate the SPDP transfer wavefront in the phase-retrieval algorithm. The result for the upper compressor, retrieved from approximately 20 low-energy shots, is displayed in Fig. 124.35. The SPDP transfer wavefront is added to all FSD wavefront measurements.

To evaluate the improvement gained by use of the SPDP transfer wavefront measurement, focal-spot measurements at the SPDP were performed with a narrowband laser¹² propagated through the beamline and through the compressor to the diagnostic table. The outer segments of the beam were obscured in order to illuminate only the central grating tile in the grating compressor (see the next section). Therefore, the pupil had a single rectangular area and the spectral width was essentially monochromatic compared to the 8-nm OPCPA spectrum.

Figure 124.36 shows how the application of the SPDP transfer wavefront improves the focal-spot prediction in this single-segment, quasi-monochromatic scenario. The cross-correlation between the FSD-generated far-field distribution and the measured intensity from the FF CCD is shown for six different shots. For each shot, the correlation before (blue diamonds) and after (red squares) applying the SPDP transfer

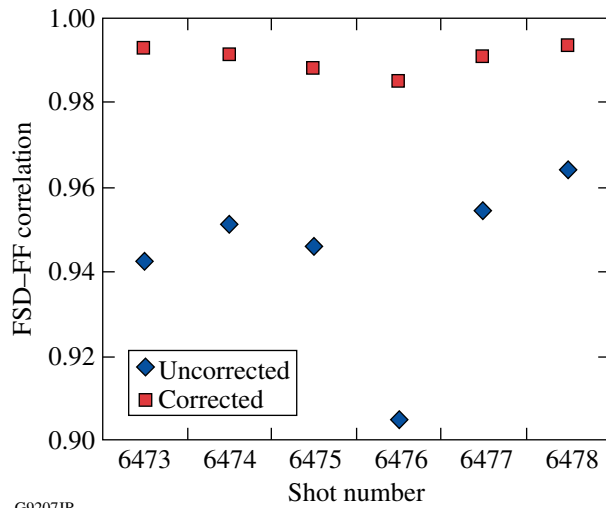
wavefront correction is shown. The correction was seen to improve the focal-spot cross-correlation from an average of 0.944 to 0.990, and the standard deviation was reduced from 0.021 to 0.003.



G9205JR

Figure 124.35

The SPDP transfer wavefront for the upper compressor. This wavefront was retrieved from a large number of shot measurements using the modal phase-retrieval algorithm with FSD wavefront sensor and FF CCD image data. The SPDP transfer wavefront was added to all FSD wavefront measurements to improve agreement with the FF CCD images.



G9207JR

Figure 124.36

The effect of the SPDP transfer wavefront on the quality of the FSD measurement is shown for the single-tile monochromatic beam. The cross-correlation between the FSD-generated far-field distribution and the measured intensity from the FF CCD is shown for six different shots. For each shot, the correlation before (blue diamonds) and after (red squares) applying the SPDP transfer wavefront correction is shown. The correction was seen to improve the correlation from an average of 0.944 to 0.990, and the standard deviation was reduced from 0.021 to 0.003.

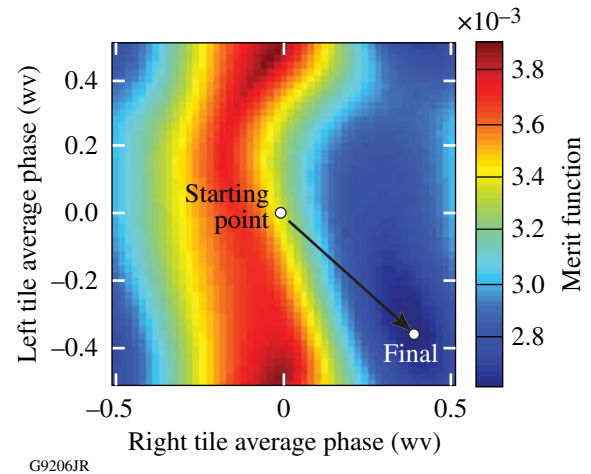
2. Single-Shot Retrieval of Average Relative Wavefront in Outer-Beam Segments

The pulse-compression system in OMEGA EP uses four tiled-grating assemblies, each comprised of three closely spaced, interferometrically aligned grating segments, to produce an effective meter-scale grating.¹³ To prevent damage associated with high-energy illumination of the edges of the grating tiles, the short-pulse beams in OMEGA EP are apodized in the region of the gaps between tiles. This produces the three-segment beam profile shown in the inset of Fig. 124.31 and further complicates the focal-spot measurement.

The FSD wavefront sensor, being a Shack–Hartmann type, fundamentally measures the local wavefront slopes across the pupil. Spatial-integration algorithms are used to reconstruct the wavefront,¹⁴ but there is an inherent uncertainty in the average wavefront in each discrete segment of the beam. This is normally not an important issue when measuring a beam with a single continuous pupil area because the overall piston phase is unimportant. In the case of OMEGA EP's three-segment beams, however, this limitation results in an inherent uncertainty in the relative average wavefront between the adjacent segments. Consequently, there is a differential piston artifact in the measurement that can significantly impact the focal-spot

prediction. Fortunately, this uncertainty can again be resolved by retrieving the relative average phase in the outer-beam segments from the FF CCD image.

Figure 124.37 shows a typical plot of the rss error merit function in Eq. (2) versus the relative piston phase (in waves) in the two outer beam segments. To retrieve the average relative wavefront in the outer segments, one searches for the minimum of the merit function in this plot. Note that the merit function has periodic boundary conditions, with one full period shown. A grid search followed by a quasi-Newton gradient-minimization search has proven to be a reliable means of finding the optimum solution for all shots encountered.



G9206JR

Figure 124.37

A typical plot of the merit function versus the piston wavefront in the outer beam segments. To retrieve the average relative wavefront in the outer segments, one searches for the minimum of the merit function in this plot. Note that the merit function has periodic boundary conditions, with one full period shown.

To test the retrieval of the relative phase in the outer beam segments, the experiment with the narrowband laser described in the previous subsection was repeated, illuminating multiple beam segments. The obscuration in the beam was removed to propagate first two, then all three beam segments through the compressor. The results of this experiment are summarized in Fig. 124.38. The plot shows the average and range of cross-correlations over six shots, illuminating one, two, and three beam segments. For each configuration, the red squares and error bars were generated with the outer-segment piston phase retrieved, while the blue diamonds were generated without performing that step (by optimizing wavefront continuity across beam segments). The error bars represent the minimum and maximum values over the six measurements. The SPDP transfer wavefront

was applied for all shots. Note that the corrected measurements remained at a high value (>0.97 for all measurements) for all the shots in this monochromatic case. Conversely, when the average relative phase in the outer segments was not retrieved, the cross-correlation and variability became progressively worse as more beam segments were introduced.

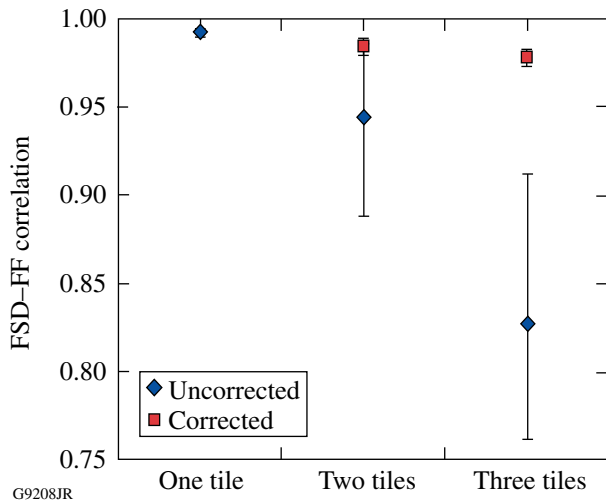


Figure 124.38

Monochromatically illuminating multiple tiles, the effect of the average relative wavefront between the beam segments is illustrated. The plot shows the average and range of correlations over six shots illuminating one, two, and three tiles. For each configuration, the correlations with (red squares) and without (blue diamonds) solving for the relative wavefront in the outer segments are shown, and the error bars represent the minimum and maximum values over six measurements. The SPDP transfer wavefront was applied for all shots. The corrected measurements remained at a high value (>0.97 for all measurements) for all three beam segments for this monochromatic case.

3. Estimating Effects of Polychromatism on Focal-Spot Structure

Despite the relatively narrow spectral widths involved (~ 8 nm unamplified and ~ 3.3 nm amplified), the short-pulse system on OMEGA EP can exhibit strong chromatic aberrations. The dominant chromatic aberration observed thus far has been attributed to residual angular dispersion, which can arise either in the stretcher or in the pulse compressor, and produces a wavelength-dependent tilt term. The polychromatism has been observed to significantly affect the far field, as demonstrated in Fig. 124.39. The focal-spot distribution in Fig. 124.39(a) shows the predicted focal-spot fluence based on monochromatic propagation of the measured near field of the FSD. The actual focal spot from the full 8-nm OPCPA bandwidth as measured by the FF CCD is shown in Fig. 124.39(b). The polychromatism is evident in the reduced sharpness of the focal spot and the peak fluence, which is lower by a factor of ~ 2 . The blurring

of the focal spot is typically along a preferential axis, which is indicative of a wavelength-dependent tilt term as expected from residual angular dispersion. Note that the blurring of the sort shown was not observed in the narrowband experiment described in the previous subsections and, consequently, cannot be explained by the modulation transfer function of the FF CCD lens.

The polychromatic blurring cannot be explained simply by the spectral content of the beam without a chromatically vary-

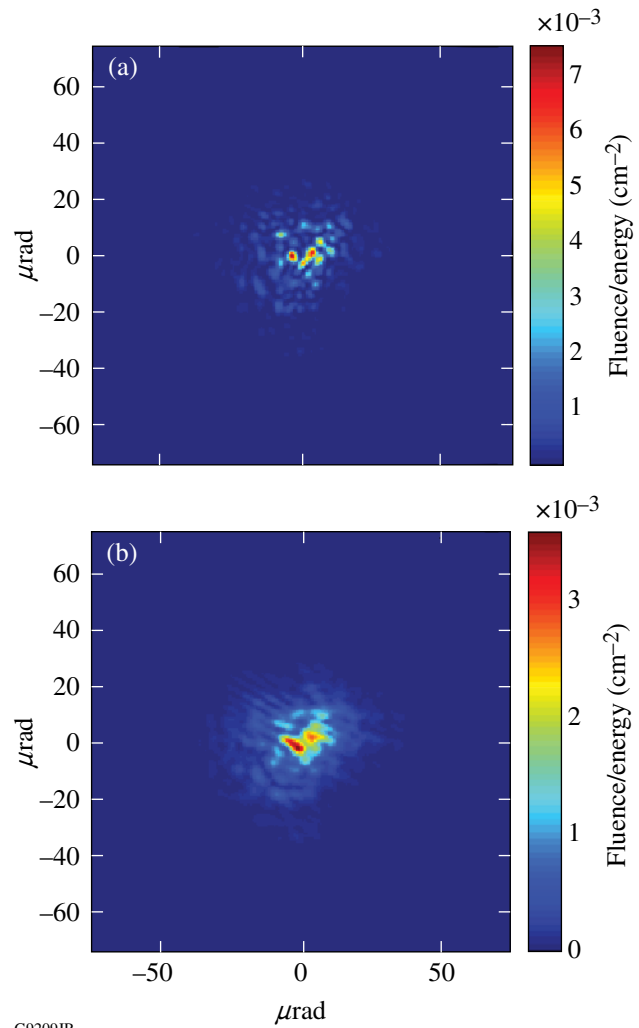


Figure 124.39

Polychromatism has been observed to blur the fine features of the far-field intensity pattern when the OPCPA beam is measured. The focal-spot distribution in (a) shows the predicted focal-spot fluence based on monochromatic propagation of the measured near field of the FSD. The actual focal spot from the full 8-nm OPCPA bandwidth as measured by the FF CCD is shown in (b). The polychromatism degrades the sharpness of the focal spot and reduces the peak fluence by approximately a factor of 2 in this case.

ing component of the wavefront. In other words, if the far field is polychromatically generated from the measured wavefront, by incoherently summing the far fields propagated from the near field using a range of wavelengths, the effect on the predicted focal spot is insignificant. The type of blurring we have observed would be seen over this narrow spectral width only if there was a significant variation in the wavefront (particularly tilt) over the spectral range.

Because the FSD wavefront sensor is not spectrally sensitive, it cannot provide information on the chromatic aberrations and, instead, produces a spectrally averaged wavefront measurement. To estimate the effects on polychromatism,

however, a Fourier analysis has been developed (Fig. 124.40). In the first step of the process, the focal-spot intensities measured by the FF CCD and monochromatically calculated from the FSD wavefront sensor are both Fourier transformed. A polychromatic transfer function is then estimated by taking the ratio of the Fourier transforms, smoothing, and fitting an elliptical Gaussian function. In the third step, the polychromatic transfer function is inverse Fourier transformed to generate a polychromatic impulse response. Finally, the original monochromatically calculated FSD focal-spot measurement is convolved with the polychromatic impulse response to obtain a focal-spot fluence distribution that includes an estimate for polychromatic effects.

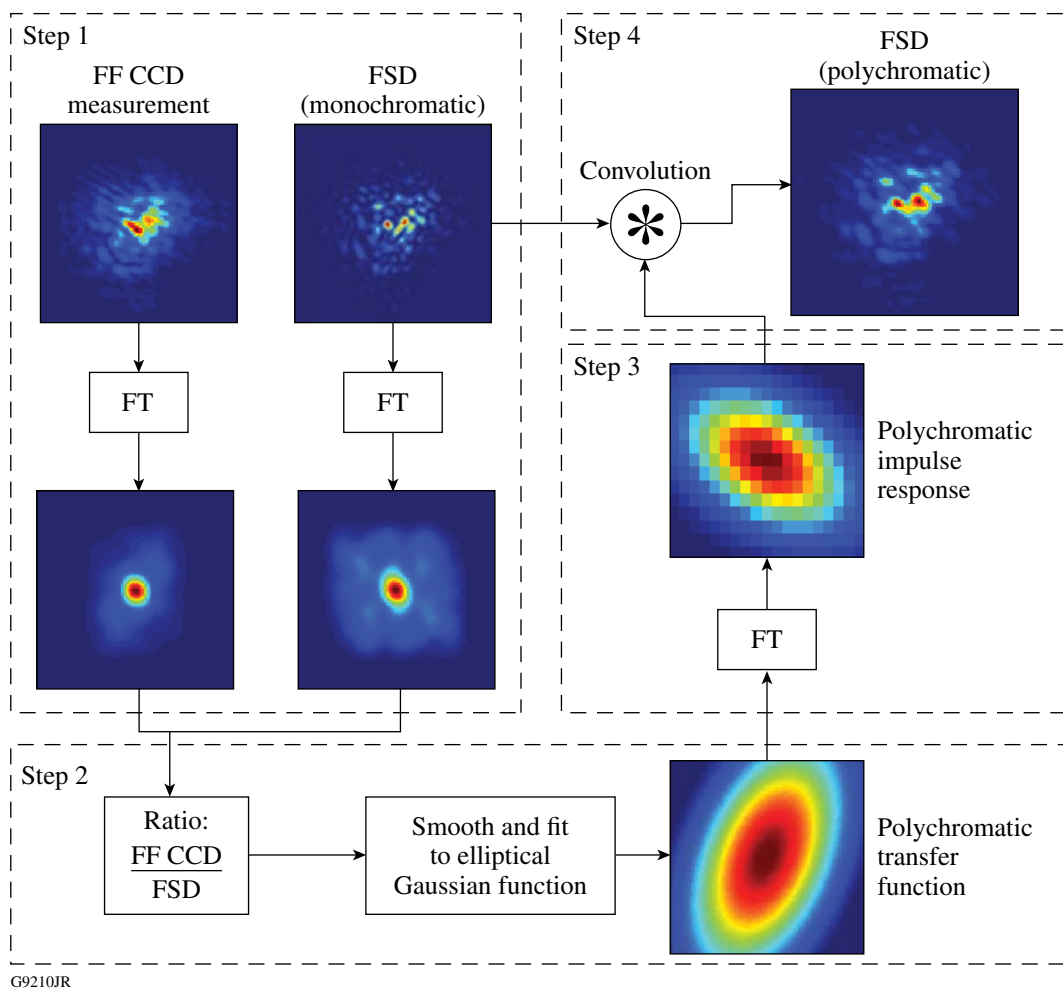


Figure 124.40

The four-step algorithm for estimating the effects of polychromatic blurring. In Step 1 of the process, the focal-spot intensities measured by the FF CCD and monochromatically calculated from the FSD wavefront sensor are Fourier transformed. In Step 2, the polychromatic transfer function is estimated by taking the ratio of the Fourier transforms from Step 1, smoothing, and fitting to an elliptical Gaussian function. The polychromatic transfer function is then inverse Fourier transformed to generate the polychromatic impulse response in Step 3. Finally, in Step 4 the original monochromatically calculated FSD focal-spot measurement is convolved with the polychromatic impulse response to obtain a focal-spot fluence distribution that includes an estimate for polychromatic effects.

We emphasize that this system provides only an *estimate* for polychromatism and is, in fact, only appropriate if residual angular dispersion is the dominant mechanism. Other sources of polychromatic error will affect the focal spot in a more-complex way than can be modeled with an intensity impulse response. For example, there is longitudinal chromatic aberration in the spatial-filter lenses in the beamline. This, in principle, is corrected using a diffractive optical element in the injection lens,¹⁵ although its performance in the system has not yet been experimentally verified. There is also a chromatic contribution associated with the spatial chirp on the beam at the second and third gratings in the compressor. The surface errors in those tiled-grating assemblies produce a wavefront error that has a wavelength-dependent horizontal displacement on the beam. These effects, which are not addressed with this method, will be a subject for further development.

4. Phase Retrieval to Improve FSD Calibration

The final issue that was addressed was the appearance of fixed errors in the calibration of the FSD wavefront sensor. It is believed that the primary source of error in the FSD calibration process is contributed by the two reference sources used in the calibration measurements. These were characterized offline and compensated as part of the calibration process, but changes in the wavefront performance of the laser sources and measurement errors both contribute to calibration errors. There also exist optical elements that are inserted into the beam path for the calibration process but removed under normal operating conditions, which could contribute fixed wavefront errors. Finally, because the FSD wavefront is effectively “transferred” to the FF CCD to use the earlier phase-retrieval techniques, any wavefront error in the far-field lens is effectively added to the

wavefront measurement. This wavefront error in the far-field lens must be removed via the transfer wavefront, introducing another error in the FSD calibration.

These fixed calibration errors were inferred using the modal phase-retrieval process described above, but this time using image data from the FSM from a number of low-energy shot campaigns. In each campaign, a series of shots was acquired with the OPCPA beam propagating through both the passive beamline and the compressor. The deformable mirror (see Fig. 124.31) was used to introduce phase diversity in the shot sequence to improve the phase-retrieval results. The FSM was inserted into the target chamber and aligned to image the focal spot at the center of the target chamber. For each shot, the techniques described earlier were used to correct the FSD wavefront measurement and to retrieve the polychromatic impulse response to obtain agreement between the FSD and the SPDP far-field CCD. The transfer wavefront measured during FSD calibration prior to each shot campaign was then applied to obtain an initial estimate for the wavefront converging to the target plane. A transfer-wavefront correction was then retrieved by using a variant of the modal phase-retrieval process described above using FSD and FSM data as inputs from a large number of shots. One key difference from the earlier modal phase-retrieval application is that the average phase in the outer beam segments was not varied when retrieving the transfer wavefront correction. These parameters were determined via phase retrieval using the FF CCD image and are therefore fixed at this stage. Furthermore, the transfer-wavefront correction is expected to be continuous over the beam aperture.

The resulting transfer-wavefront corrections (Fig. 124.41) have been evaluated for three different target configurations:

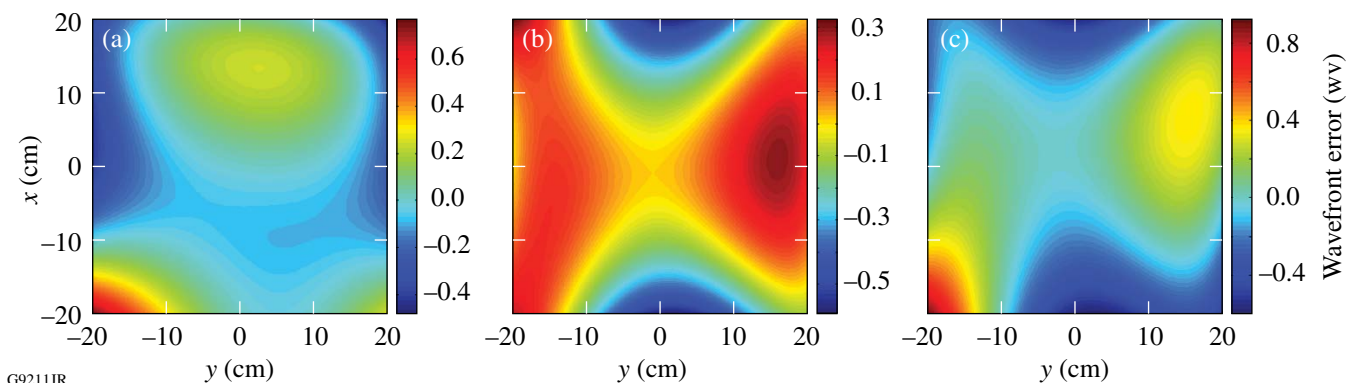


Figure 124.41

Transfer-wavefront corrections are shown for (a) upper compressor to the OMEGA EP backlighter, (b) lower compressor to the OMEGA EP sidelighter, and (c) upper compressor to the OMEGA backlighter. These were retrieved from low-energy shot campaigns using FSM measurements in conjunction with FSD wavefront measurements using a phase-retrieval process similar to that shown in Fig. 124.34. These correction wavefronts were applied to all FSD calibration measurements obtained using the technique in Fig. 124.32.

(a) the upper compressor propagating to the backlighter OAP in the OMEGA EP target chamber, (b) the lower compressor to the OMEGA EP sidelighter OAP, and (c) the upper compressor to the OMEGA target chamber OAP. As before, the correction wavefront is estimated by a fourth-order Legendre polynomial. It is important to also note that the transfer-wavefront correction has been confirmed to be reasonably stable over multiple shot campaigns conducted over approximately one year. The transfer-wavefront correction measurements will be performed periodically in the future to confirm its stability or adapt to changes in the system performance. Variability observed in the transfer-wavefront correction is used to estimate the uncertainty of the target-plane measurement.

Note that special consideration must be made for defocus when measuring the transfer-wavefront correction. In shot campaigns in general, defocus within the target chamber is an unknown parameter, affected by both the positioning of the OAP and the target itself. Furthermore, during the FSD calibration, longitudinal errors in the placement of the in-tank source will lead to a defocus error. Finally, during the FSM shot campaigns, errors in alignment of the FSM to the OAP focal plane led to defocus in the measured focal spot that introduced a defocus term into the transfer-wavefront correction via the phase-retrieval process. To deal with the defocus uncertainty, a through-focus scan was conducted as part of each FSM shot campaign to measure the FSM defocus relative to the OAP. As a result, defocus was effectively removed from the transfer-wavefront correction.

Results

To evaluate the performance of the phase-retrieval techniques described in the previous section, they have been applied to a number of on-shot focal-spot measurements and compared to available direct focal-spot measurements. First, the accuracy of the sample-beam focal-spot measurement is considered by comparing the FSD result with the FF CCD.

As an example of the impact of these phase-retrieval improvements, the sample-beam focal-spot measurement shown in Fig. 124.33 is again considered in Fig. 124.42. The direct focal-spot measurement from the FF CCD camera is repeated in Fig. 124.42(a). The far-field fluence calculated using near-field measurements by the FSD wavefront sensor, including correction for the SPDP transfer wavefront, the average phase in the outer beam segments, and estimation of polychromatic effects, is shown in Fig. 124.42(b). The corrected FSD prediction shows a much-better qualitative correspondence with the direct FF CCD measurement than the uncorrected

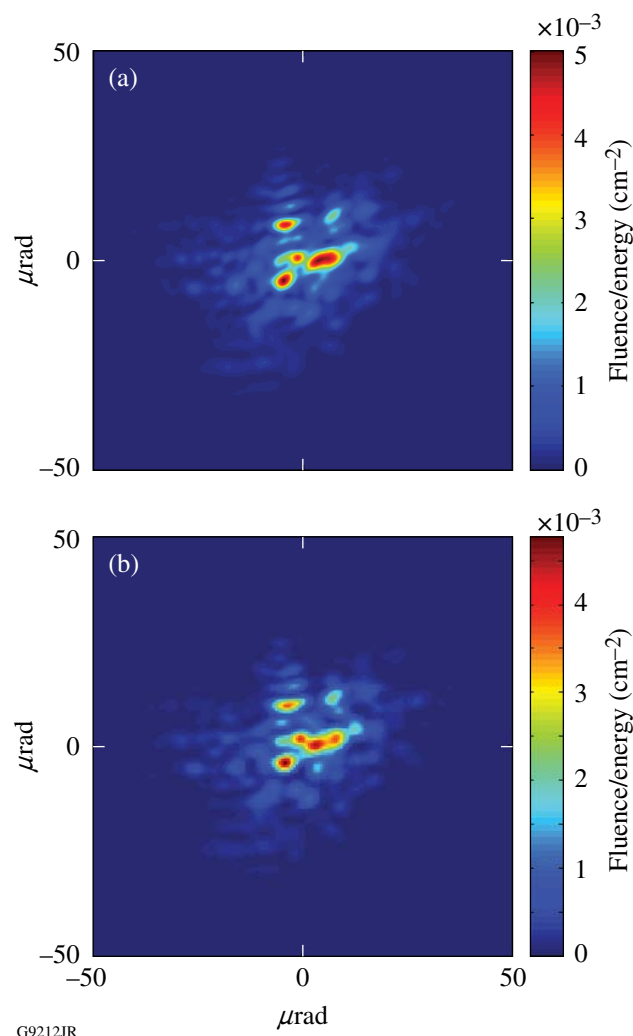


Figure 124.42

The sample-beam focal-spot measurement shown in Fig. 124.33 is repeated here using the phase-retrieval techniques described. (a) The direct focal-spot measurement from the FF CCD camera. (b) The far-field fluence calculated using near-field measurements by the FSD wavefront sensor, including correction for the SPDP transfer wavefront, the average phase in the outer beam segments, and estimation of polychromatic effects. The two focal-spot agreements match much better qualitatively than the uncorrected case shown in Fig. 124.33. The quantitative agreement is also much better, with the cross-correlation improving from 0.71 to 0.95.

case shown in Fig. 124.33. The quantitative agreement is also much better, with the cross-correlation improving from 0.71 to 0.95. The prediction of the peak intensity has also improved to within 10% accuracy, compared to the initial estimate that overpredicted the peak intensity by $>2\times$.

The improved focal-spot measurement of the sample beam has also proven to be very reliable and stable over a large number of shots. To illustrate this, the cross-correlation has been

evaluated over a population of 175 low-energy shots, which spanned approximately 18 months. Figure 124.43 is a histogram showing the frequency of cross-correlations within intervals of 0.01. The filled bars correspond to the corrected measurements, i.e., when the SPDP transfer wavefront (assumed static over the entire time period), the average phase in the outer segments, and the effects of polychromatism have all been applied. The white bars give the cross-correlation values without these corrections. There is a clear improvement in performance after applying the phase-retrieved corrections, with the mean cross-correlation increasing from 0.826 to 0.965. The consistency of the measurement was also much improved, with the standard deviation of the cross-correlation reduced from 0.044 to 0.010.

Amplifying the beam did not adversely affect the quality of focal-spot measurement, as demonstrated in the histogram in Fig. 124.44. The cross-correlation between the FSD and the FF CCD was calculated after applying all the phase-retrieved corrections. The white bars represent the rate of occurrence for each cross-correlation value for all high-energy shots over a recent 6-month period, representing a population of 220 samples. The filled bars represent the same data for all the low-energy FSM campaign shots evaluated in Fig. 124.43. The statistics are quite similar: the low-energy and high-energy mean cross-correlations are 0.965 and 0.967, respectively, which are effectively identical considering the standard deviations (0.010 and 0.009, respectively).

To achieve consistent performance over the wide range of shot conditions included in this study, it was necessary to account for changes in the system configuration in the diagnostic package. Specifically, wavefront contributions from neutral-density filters inserted in front of the FSD wavefront sensor can be significant. The wavefront introduced by each of these filters is characterized *in situ* in an offline measurement and removed from each on-shot wavefront measurement as appropriate.

The true test of the FSD measurement accuracy is its ability to accurately measure the focal spot remotely in the target chamber. The cross-correlation between the FSD focal-spot prediction and the direct measurement using the FSM was evaluated for all the low-energy shot campaigns described earlier. A histogram of the cross-correlation data is presented in Fig. 124.45. The histogram in Fig. 124.45(a) shows the effect of the phase-retrieval corrections on the focal-spot measurement. The white bars give the distribution of cross-correlation values between the FSD and direct FSM measurements when no phase-retrieval corrections have been applied. The filled bars, which show the corresponding cross-correlations with the addition of the phase-retrieval corrections, demonstrate the improvement in overall quality and reliability. The histogram in Fig. 124.45(b) compares the quality of the measurement of the sample beam at the SPDP table (filled bars) and the main beam in the target chamber (white bars). All phase-retrieval corrections were applied for this data. The measurement accuracy

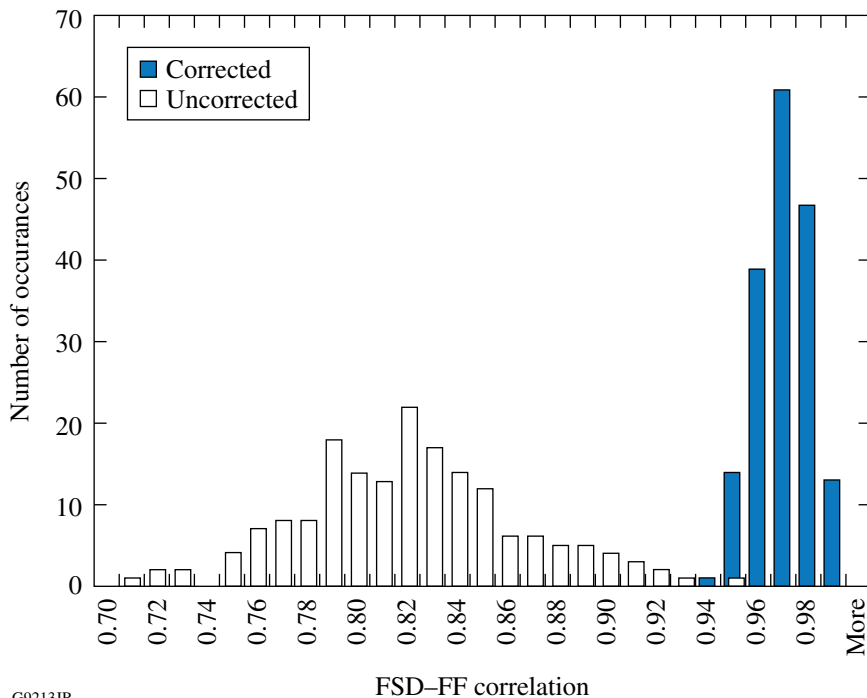


Figure 124.43

A histogram of the cross-correlations between the FSD and FF CCD measurements. The filled bars give the values when the SPDP transfer wavefront, the average phase in the outer segments, and the effects of polychromatism have all been retrieved. The white bars give the values without these corrections. The histograms consist of low-energy shots with the full OPCPA bandwidth, acquired during the shot campaigns to the FSM, which spanned approximately 18 months.

G9213JR

is slightly worse in the target chamber, likely because of the variability in the transfer-wavefront correction from campaign to campaign; however, the measured cross-correlation reliably exceeds 0.9 with >95% probability.

Unfortunately, confirming an accurate measurement of the focal-spot measurement at high energy is currently not possible since a high-energy shot cannot be sufficiently attenuated to the level required for the focal-spot microscope. Other target

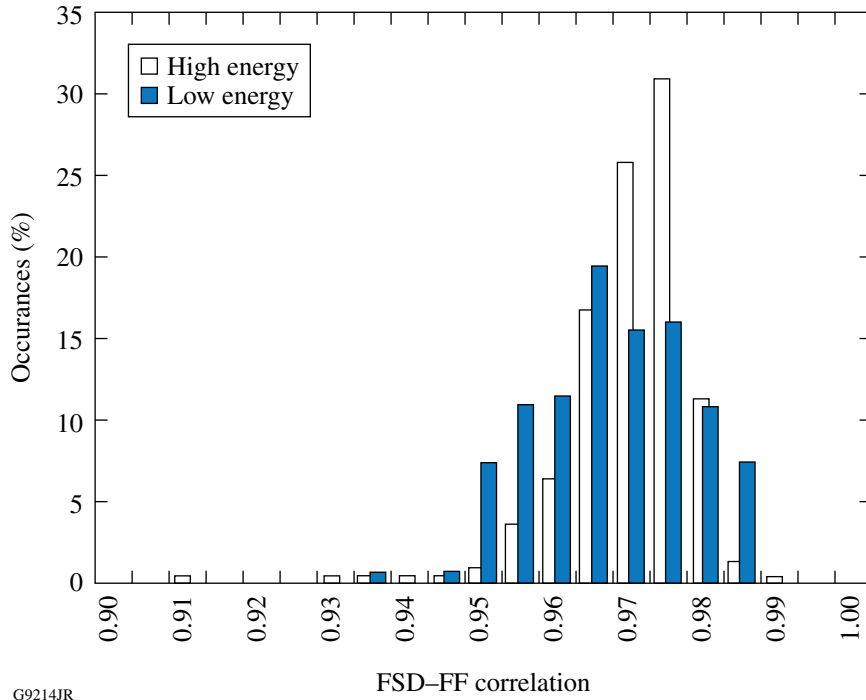
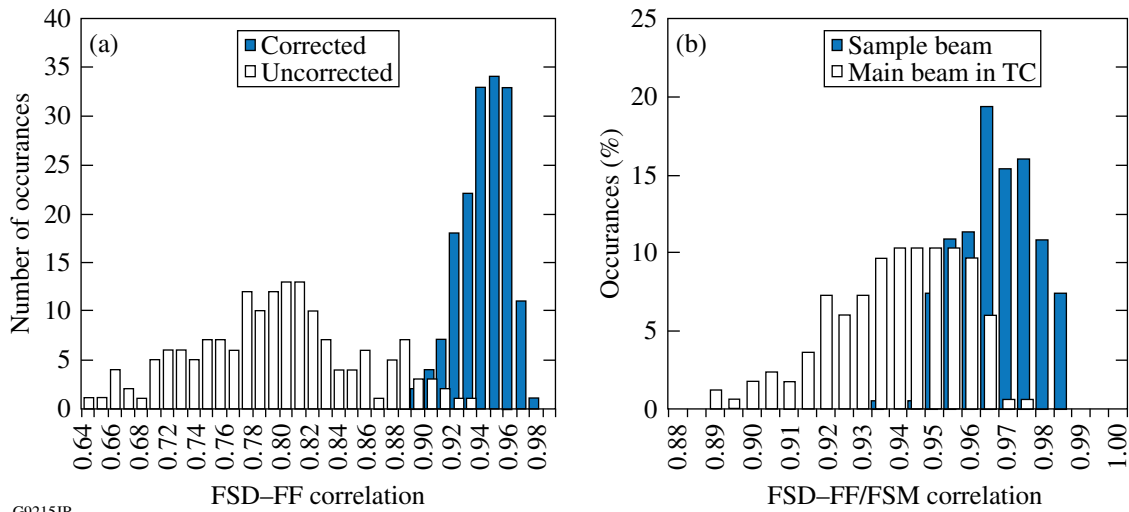


Figure 124.44

A histogram demonstrating that the consistently high sample-beam focal-spot measurement accuracy is maintained for high-energy OMEGA EP shots. The white bars represent the rate of occurrence for each cross-correlation between the FSD and the far-field CCD for all high-energy shots over a recent 6-month period. The filled bars represent the same data for all the low-energy FSM campaign shots, as also plotted in Fig. 124.43. The values are calculated with all phase-retrieved corrections.

G9214JR



G9215JR

Figure 124.45

The accuracy of the focal-spot measurement of the main beam in the target chamber is evaluated in the histograms. (a) The effect of the phase-retrieval corrections on the focal-spot measurement. The white bars give the distribution of cross-correlation values between the FSD and direct FSM measurements when no phase-retrieval corrections have been applied. The filled bars, which show the corresponding cross-correlations with the addition of the phase-retrieval corrections, demonstrate the improvement in overall quality and reliability. (b) A comparison of the quality of the measurement of the sample beam at the SPDP table (filled bars) and the main beam in the target chamber (TC) (white bars). All phase-retrieval corrections were applied for this data. The measurement accuracy is slightly worse in the target chamber, likely because of the variability in the transfer-wavefront correction from campaign to campaign.

diagnostics, such as x-ray pinhole cameras, have poor resolution and do not provide a true measure of focal-spot fluence because of the complexities of the target interaction. For this reason we must rely on the low-energy results to assess the performance of the focal-spot measurement at the target plane. To maximize the confidence in the measurement at high energy, we have accounted for all changes to the system configuration for these shots, e.g., attenuators inserted before the SPDP. The wavefront errors contributed by all configuration changes were measured individually offline. On high-energy shots, the wavefront contributed by each inserted aberrator was removed from the measurement to correct for potential measurement error.

Conclusions

Phase retrieval has been a useful technique for obtaining consistently high quality remote predictions of the on-shot target-plane fluence distribution. A modal phase-retrieval technique based on a gradient-search algorithm was used to retrieve correction wavefronts for the FSD that produce focal spots in consistent agreement with direct measurements of the sample beam and main beam at the target plane for low energy. Phase retrieval was also used to provide phase information beyond the capabilities of the Shack–Hartmann wavefront sensor. The relative piston phase between the discrete segments of the OMEGA EP beam was retrieved on each shot using an image of the sample-beam focal spot. Further, an estimate of the effects of chromatic aberration on the focal-spot fluence distribution was obtained from the sample-beam focal-spot image using a Fourier technique.

Analysis of a large population of on-shot measurements has proven the focal-spot measurement to be reliable. Cross-correlation with direct focal-spot fluence measurements using the far-field CCD and the FSM consistently exceeded 90%, although no direct measurement at the target plane at high energy is currently possible.

As a result of the improved accuracy of the on-shot focal-spot measurement, scientists conducting experiments on the OMEGA EP short-pulse beamlines now have critical information about on-target intensity distributions. This information is proving to be very useful and is enhancing the value of OMEGA EP experiments for furthering our understanding of ICF physics.

ACKNOWLEDGMENT

The authors thank Prof. James Fienup for insightful discussions on phase-retrieval algorithms. This work was supported by the U.S. Department of Energy Office of Inertial Confinement Fusion under Cooperative Agreement No. DE-FC52-08NA28302, the University of Rochester, and the New York State Energy Research and Development Authority. The support of DOE does not constitute an endorsement by DOE of the views expressed in this article.

REFERENCES

1. J. H. Kelly, L. J. Waxer, V. Bagnoud, I. A. Begishev, J. Bromage, B. E. Kruschwitz, T. J. Kessler, S. J. Loucks, D. N. Maywar, R. L. McCrory, D. D. Meyerhofer, S. F. B. Morse, J. B. Oliver, A. L. Rigatti, A. W. Schmid, C. Stoeckl, S. Dalton, L. Folnsbee, M. J. Guardalben, R. Jungquist, J. Puth, M. J. Shoup III, D. Weiner, and J. D. Zuegel, *J. Phys. IV France* **133**, 75 (2006).
2. J. Bromage, S.-W. Bahk, D. Irwin, J. Kwiatkowski, A. Pruyne, M. Millecchia, M. Moore, and J. D. Zuegel, *Opt. Express* **16**, 16,561 (2008).
3. R. W. Gerchberg and W. O. Saxton, *Optik* **35**, 237 (1972).
4. R. A. Gonsalves, *J. Opt. Soc. Am.* **66**, 961 (1976).
5. J. R. Fienup, *Appl. Opt.* **21**, 2758 (1982).
6. J. R. Fienup, *Appl. Opt.* **32**, 1737 (1993).
7. S.-W. Bahk, J. Bromage, I. A. Begishev, C. Mileham, C. Stoeckl, M. Storm, and J. D. Zuegel, *Appl. Opt.* **47**, 4589 (2008).
8. Imagine Optic, 91400 Orsay, France (<http://www.imagine-optic.com/>).
9. J. W. Goodman, *Introduction to Fourier Optics* (McGraw-Hill, New York, 1968).
10. C. G. Broyden, *IMA J. Appl. Math.* **6**, 76 (1970); R. Fletcher, *Comput. J.* **13**, 317 (1970); D. Goldfarb, *Math. Comput.* **24**, 23 (1970); D. F. Shanno, *Math. Comput.* **24**, 647 (1970).
11. S. Kirkpatrick, C. D. Gelatt, Jr., and M. P. Vecchi, *Science* **220**, 671 (1983).
12. A Q-switched diode-pumped Nd:YLF laser from Photonics Industries was used, model DS10-1053; Photonics Industries International, Inc., Bohemia, NY 11716 (<http://www.photonix.com>).
13. J. Qiao, A. Kalb, T. Nguyen, J. Bunkenburg, D. Canning, and J. H. Kelly, *Opt. Lett.* **33**, 1684 (2008).
14. cf. D. L. Fried, *J. Opt. Soc. Am.* **67**, 370 (1977); this work used the method described in S.-W. Bahk, *Opt. Lett.* **33**, 1321 (2008).
15. T. J. Kessler, H. Huang, and D. Weiner, in *International Conference on Ultrahigh Intensity Laser Development, Science and Emerging Applications 2006* (ICUIL, Cassis, France, 2006), pp. 126–128.